Supplementary materials for

A multiple asymmetric bilateral rupture sequence derived from the peculiar tele-seismic P-waves of the 2025 Mandalay, Myanmar earthquake

Naohiro Inoue[1], Ryo Yamaguchi[1], Yuji Yagi[2], Ryo Okuwaki[2], Bogdan Enescu[3,4], and Tira Tadapansawut[5]

[1]Graduate School of Science and Technology, University of Tsukuba, Tennodai 1-1-1, Tsukuba, Ibaraki 305– 8572, Japan

[2]Institute of Life and Environmental Sciences, University of Tsukuba, Tennodai 1-1-1, Tsukuba, Ibaraki 305– 8572, Japan

[3]Department of Geophysics, Graduate School of Science, Kyoto University, Kitashirakawa, Oiwake-cho, Sakyo-ku, Kyoto 606-8502, Japan

[4]National Institute for Earth Physics, Calugareni str. 12, P.O. Box MG-2, 077125, Magurele-Bucharest, Ilfov, Romania

[5]College of Integrated Science and Technology, Rajamangala University of Technology Lanna, 128 Huay Kaew Road, Muang, Chiang Mai, 50300, Thailand

Contents:

Text S1

In this study, we introduced the uncertainty of the Green's function into the data covariance matrix, and estimated the hyperparameters using ABIC (Akaike, 1980), thereby achieving stable and detailed estimation of the seismic source process with a high-degree-of-freedom model (Yagi and Fukahata, 2011, Shimizu et al., 2020). However, our approach cannot evaluate the effect of non-Gaussian modeling errors resulting from the model settings. Here, we tested our modeling using multiple different model settings and evaluated the robustness of the results.

First, in order to evaluate the effect of the velocity structure setting on the inversion results, we used four different velocity structures (Tables S2–S5) from CRUST1.0's 1x1-degree cells (Laske et al., 2013) around the seismic source region: the northeast model (cell center: 21.5°N, 96.5°E), the northwest model (cell center: 21.5°N, 95.5°E), southeast model (cell center: 20.5°N, 96.5°E) and southwest model (cell center: 20.5°N, 95.5°E). Although the other model settings were set at the same values as used for the optimum analysis, we only changed the velocity structures to conduct inversion. Fig. S2 shows the spatiotemporal evolution of the potency-rate density using different model settings. Using four different velocity structures it was found that the characteristics of E1 were well reproduced. For example, all models show that after the initial rupture propagated to the south, at 8 s from the origin time (OT) the rupture propagated asymmetrically in a bilateral way to the north and south. In addition, the characteristics of E2 were also reproduced, for example the feature showing the rupture started around 120 km south of the hypocenter, and propagated asymmetrically in a bilateral way to the south and north, as well as the feature showing the potency-rate density was relatively large throughout the E2 rupture region from OT+45 s to OT+58 s. When using the two velocity structures on the west side, the potency-rate density was high at the start of the rupture of the E2 episode. In addition, the estimates of the rupture area after OT+60 seconds tend to be sensitive to the velocity structure settings.

Next, in order to evaluate the effect of the model plane assumption on the inversion results, we performed an inversion with an alternative model plane inclination (dip angle) of 90° and an inversion with the hypocentral depth set to 10 km. Similar to the above structural model examination, the rupture propagation behavior of E1 and E2 were reproduced, but the characteristics of the potency rate distribution after OT+60 s varied depending on the model setting.

Finally, we set the knot interval of the potency-rate density function to 1.0 second and the input observed waveforms with a sampling interval of 1.0 s. In this case, the behavior of the rupture propagation in E1 and E2 were reproduced, but the rupture area after OT+60 seconds varied depending on the setting.

In summary, the examination using the seven alternative models considered in this study showed that the rupture propagation behavior in E1 and E2 were robustly estimated, while it was clear that the spatial distribution of the potency-rate density after OT+60 seconds could not be stably estimated.

Comparing the potency density tensor distributions on the map obtained by integrating the potency-rate density tensors (Fig. S3), it is confirmed that the areas with high potency density commonly exist from 21.5°N to 22.25°N and from 20.5°N to 21.25°N in all results. The strike direction of the potency density tensors shows the counterclockwise rotation from north to south of the model domain in all results. The feature that the dip of the north-south nodal plane is around 60° in the rupture area of E1 and around 80° in the rupture areas of E2 and E3 is reproduced even with different model settings. These results show that the potency density tensors distribution and the change of dip angle along strike direction are robustly reproduced.

Table S1: Structure from AK135-F (Kennett et al., 1995; Montagner and Kennett, 1996) used for calculating Green's functions

V_P (km/s)	V_S (km/s)	Density (10^3 kg/m^3)	Thickness (km)
5.80	3.46	2.45	20.00
6.50	3.85	2.71	15.00
8.04	4.48	3.30	- (Moho)

Table S2: The northeast structure model (cell center: 21.5°N, 96.5°E) from CRUST1.0 (Laske et al., 2013) used for calculating Green's functions

V_P (km/s)	V_S (km/s)	Density (10^3 kg/m^3)	Thickness (km)
6.10	3.55	2.74	14.80
6.30	3.65	2.78	13.61
7.00	3.99	2.95	5.93
8.01	4.45	3.30	- (Moho)

Table S3: The northwest structure model (cell center: 21.5°N, 95.5°E) from CRUST1.0 (Laske et al., 2013) used for calculating Green's functions

V_P (km/s)	V_S (km/s)	Density (10^3 kg/m^3)	Thickness (km)
2.50	1.07	2.11	0.34
4.00	2.13	2.37	4.00
5.00	2.88	2.54	1.00
5.90	3.44	2.67	10.04
6.30	3.62	2.74	9.73
6.90	3.87	2.91	9.73
8.06	4.48	3.32	- (Moho)

Table S4: The southeast structure model (cell center: 20.5°N, 96.5°E) from CRUST1.0 (Laske et al., 2013) used for calculating Green's functions

V_P (km/s)	V_S (km/s)	Density (10^3 kg/m^3)	Thickness (km)
6.10	3.55	2.74	14.65
6.30	3.65	2.78	13.61
7.00	3.99	2.95	5.94
7.96	4.43	3.28	- (Moho)

Table S5: The southwest structure model (cell center: 20.5°N, 95.5°E) from CRUST1.0 (Laske et al., 2013) used for calculating Green's functions

V_P (km/s)	V_S (km/s)	Density (10^3 kg/m^3)	Thickness (km)
2.50	1.07	2.11	0.23
4.00	2.13	2.37	4.00
5.00	2.88	2.54	2.50
5.90	3.44	2.67	9.52
6.30	3.62	2.74	9.24
6.90	3.87	2.91	9.24
8.02	4.46	3.31	- (Moho)

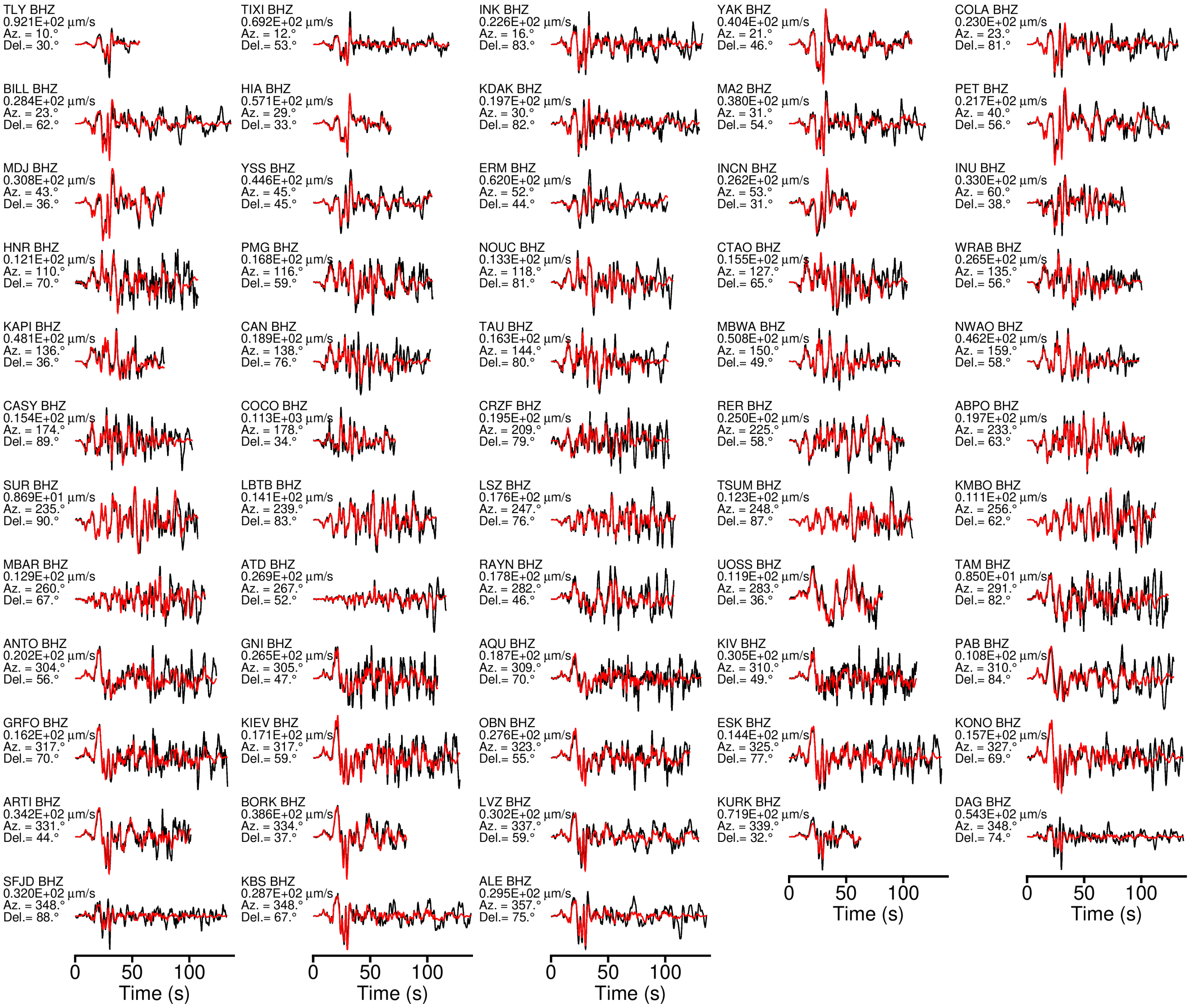

Figure S1. Observed (black) and synthetic (red) waveforms calculated from the optimum model. The station code and channel, maximum amplitude of observed data, station azimuth (Az.) and epicentral distance (Del.) are on the left of each panel. The sampling interval for all waveforms is 0.05 s, and an anti-aliasing filter is applied.

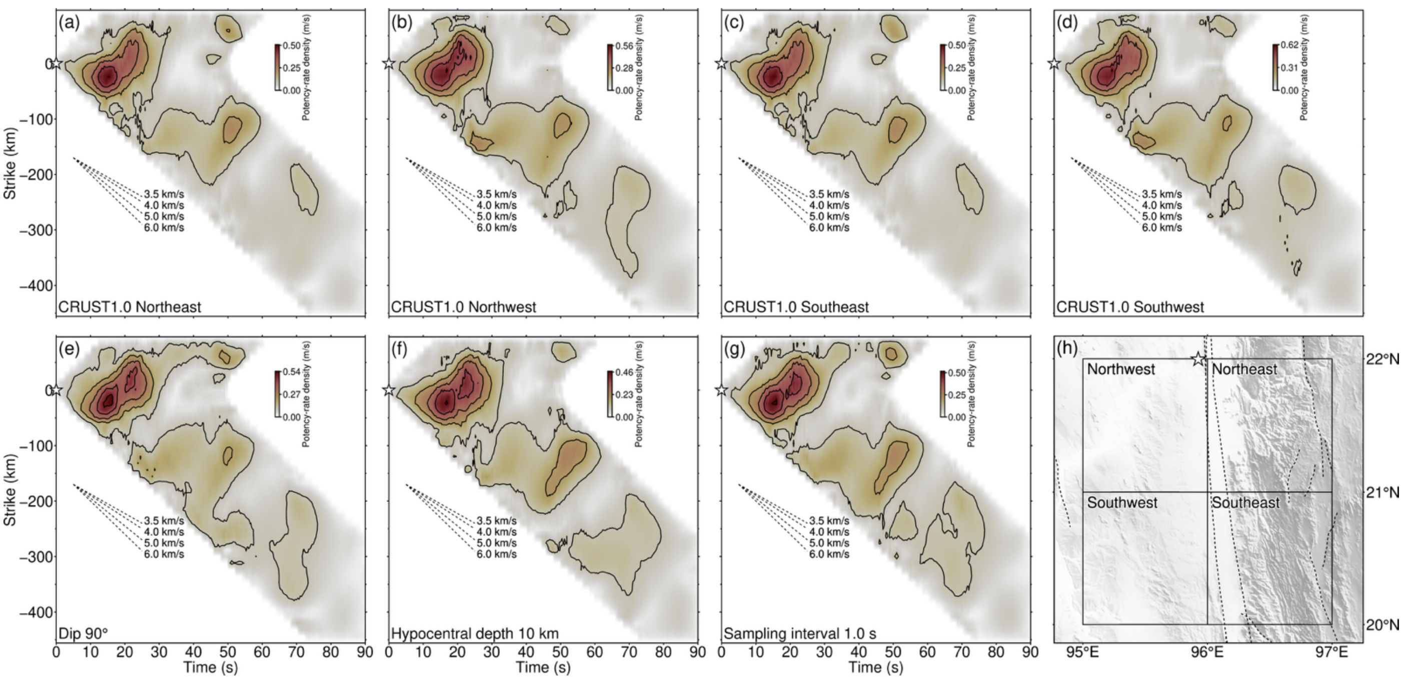

Figure S2. Compilation of potency-rate density evolution from the sensitivity test (Text S1). The star shows the initial rupture point. The dashed lines are the reference rupture speeds. (a–d) The solutions using the alternative structural models (Tables S2–S5). (e) The solution using the alternative model plane setting (90° dip). (f) The solution using the alternative initial rupture depth (10 km). (g) The solution using the alternative sampling interval (1.0 s). (h) The CRUST1.0's 1x1-degree cells (Laske et al., 2013) when selecting the alternative structure models (Tables S2–S5). The dashed lines show the active faults (Styron and Pagani, 2020). The background topography is from SRTM15+V2 (Tozer et al., 2019).

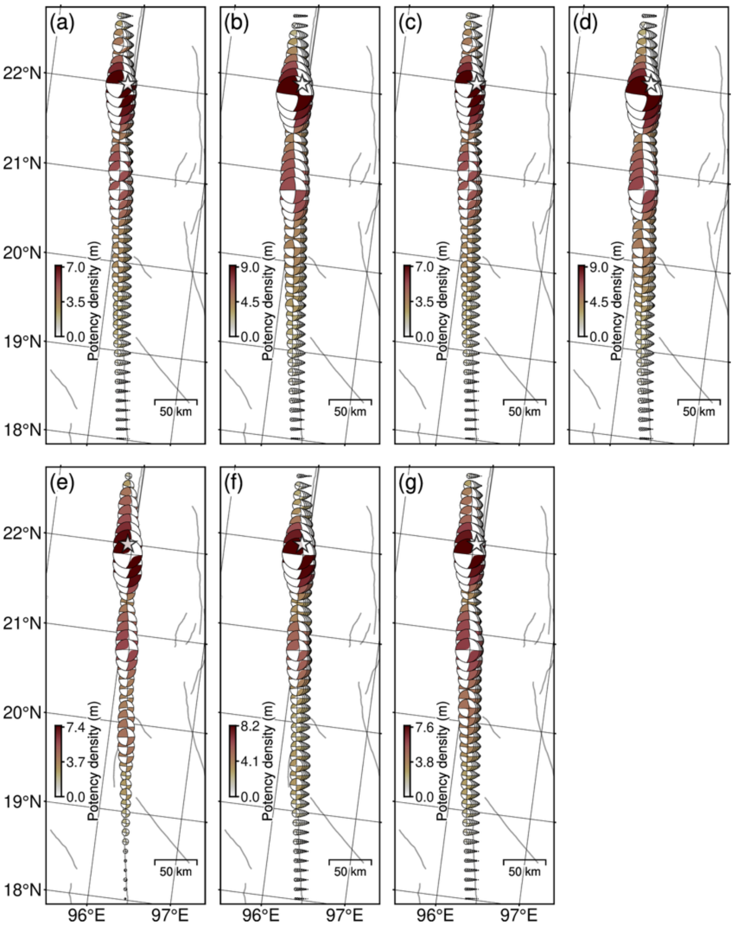

Figure S3. Compilation of potency density tensor distributions from the sensitivity test (Text S1). The star shows the initial rupture point. The lines show the active faults (Styron and Pagani, 2020). (a–d) The solutions using the alternative structural models (Tables S2–S5). (e) The solution using the alternative model plane setting (90° dip). (f) The solution using the alternative initial rupture depth (10 km). (g) The solution using the alternative sampling interval (1.0 s).

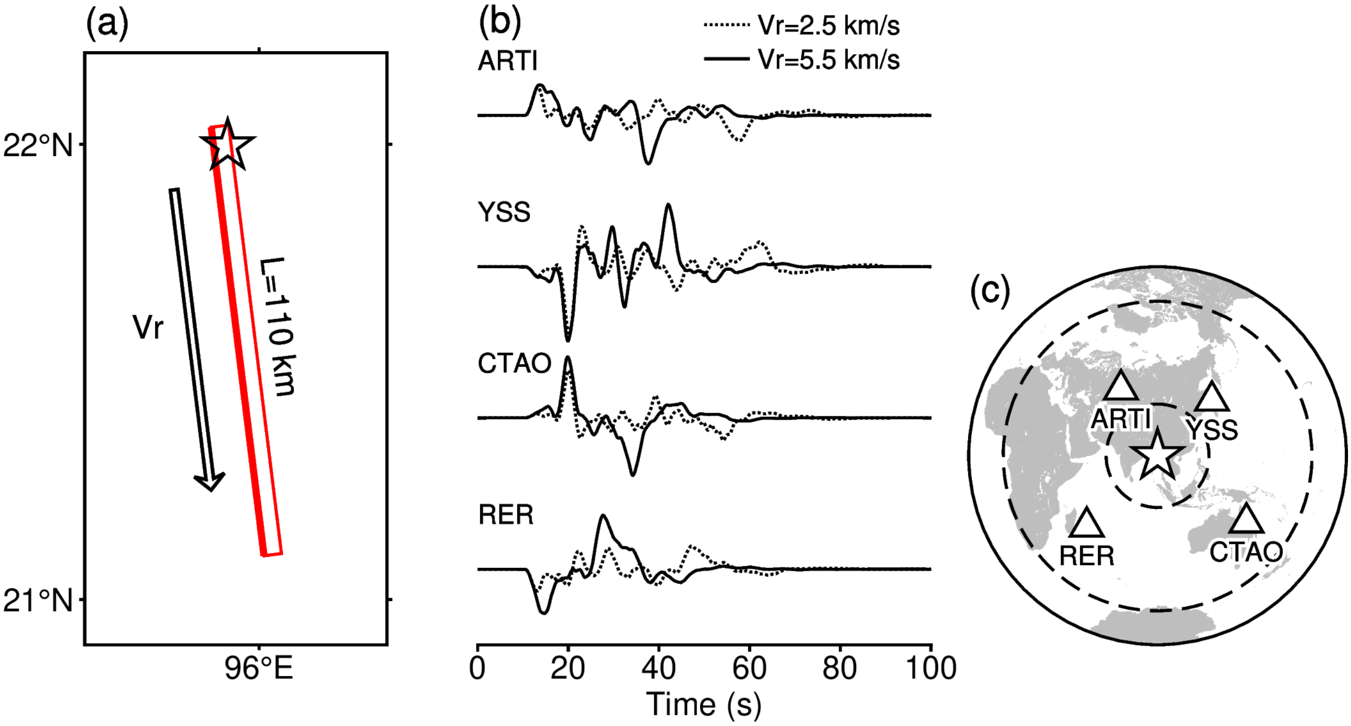

Figure S4. Comparison of the synthetic waveforms generated from the synthetic test adopting different rupture speed scenarios. (a) A schematic diagram of the model setting for the synthetic test. The star indicates the epicenter. The red rectangle shows the model plane with the thicker line representing the model top. The vector is the direction of the southward rupture propagation. For calculating the synthetic waveforms, we set the fault with length of 110 km and width of 20 km. The focal depth of the hypocenter was 18 km, and the strike, dip and rake of the fault plane are 353°, 80° and 180°, respectively. Uniform slip distribution with random noises and southern unilateral rupture are assumed on the fault plane. The rise time of each node is 5 s. We use the ak135 model (Kennett et al., 1995; Montagner and Kennett, 1996) as the velocity structure model. (b) The dashed and solid lines show the synthetic waveforms calculated with assumed rupture front speeds of 2.5 and 5.5 km/s, respectively. The sampling rate of all waveforms is 0.05 s. (c) The station distribution (triangles) corresponding to the traces in Fig. S4 (b).

References

Akaike, H., 1980. Likelihood and the Bayes procedure. Trabajos de Estadistica Y de Investigacion Operativa, 31(1), 143–166. https://doi.org/10.1007/BF02888350

Kennett, B.L.N., Engdahl, E.R., Buland, R., 1995. Constraints on seismic velocities in the Earth from traveltimes. Geophysical Journal International 122, 108–124. https://doi.org/10.1111/j.1365-246X.1995.tb03540.x

Laske, G., Masters, G., Ma, Z., Pasyanos, M., 2013. Update on CRUST1.0 - A 1-degree Global Model of Earth's Crust EGU2013-2658.

Montagner, J.-P., Kennett, B.L.N., 1996. How to reconcile body-wave and normal-mode reference earth models. Geophysical Journal International 125, 229–248. https://doi.org/10.1111/j.1365-246X.1996.tb06548.x

Shimizu, K., Yagi, Y., Okuwaki, R., Fukahata, Y., 2020. Development of an inversion method to extract information on fault geometry from teleseismic data. Geophysical Journal International 220, 1055–1065. https://doi.org/10.1093/gji/ggz496

Styron, R., Pagani, M., 2020. The GEM Global Active Faults Database. Earthquake Spectra 36, 160–180. https://doi.org/10.1177/8755293020944182

Tozer, B., Sandwell, D. T., Smith, W. H. F., Olson, C., Beale, J. R., and Wessel, P. 2019. Global Bathymetry and Topography at 15 Arc Sec: SRTM15+. Earth and Space Science, 6(10), 1847–1864. https://doi.org/10.1029/2019EA000658.

Yagi, Y., Fukahata, Y., 2011. Introduction of uncertainty of Green's function into waveform inversion for seismic source processes: Uncertainty of Green's function in inversion. Geophysical Journal International 186, 711–720. https://doi.org/10.1111/j.1365-246X.2011.05043.x